To appear in the *Journal of Geophysical Research*, 2000.

Separation of atmospheric and surface spectral features in Mars Global Surveyor Thermal Emission Spectrometer (TES) spectra

Michael D. Smith
NASA Goddard Space Flight Center, Greenbelt, Maryland

Joshua L. Bandfield and Philip R. Christensen
Department of Geology, Arizona State University, Tempe

Abstract

We present two algorithms for the separation of spectral features caused by atmospheric and surface components in Thermal Emission Spectrometer (TES) data. One algorithm uses radiative transfer and successive least squares fitting to find spectral shapes first for atmospheric dust, then for water-ice aerosols, and then, finally, for surface emissivity. A second independent algorithm uses a combination of factor analysis, target transformation, and deconvolution to simultaneously find dust, water ice, and surface emissivity spectral shapes. Both algorithms have been applied to TES spectra, and both find very similar atmospheric and surface spectral shapes. For TES spectra taken during aerobraking and science phasing periods in nadir-geometry these two algorithms give meaningful and usable surface emissivity spectra that can be used for mineralogical identification.

1. Introduction

One of the principal scientific objectives of the Thermal Emission Spectrometer (TES) investigation is to determine the composition and distribution of surface materials [*Christensen et al.*, 1992]. To do this, one needs to retrieve surface emissivity spectra from the TES spectra. However, this is not a simple process. The spectral radiance that the TES observes is a blackbody of the surface temperatures modified by the surface emissivity and by atmospheric absorption, scattering, and radiation. Because a combination of factors combine to form the one final observed quantity (spectral radiance), it is difficult to determine the relative contributions of surface emissivity and atmospheric opacity to observed spectral features.

The TES spectra contain strong atmospheric spectral features that yield a wealth of information about the state of the atmosphere [see *Christensen et al.*, 1998; *Conrath et al.*, this issue; *Smith et al.*, this issue; and J. C. Pearl et al., Mars water ice clouds: Observations by the Thermal Emission Spectrometer (TES) during the first Martian year, submitted to *Journal of Geophysical Research*, 1999 (hereinafter referred to as submitted manuscript, 1999)]. These atmospheric spectral features are often larger than those caused by non-unit surface emissivity. This is especially true of atmospheric dust. The spectral signature of atmospheric dust has similarities with those of possible silicate materials on the surface, which further complicates the separation of surface and atmosphere contributions. Because of the amount of atmospheric information in these spectra and the similarity of atmospheric features to possible surface features, great care must be taken in the determination and analysis of surface emissivity spectra.

Because of the heavy influence of dust and water-ice aerosols on infrared spectra, few studies have attempted to interpret surface features in the thermal infrared. Characterization of atmospheric effects has been hampered by the limited spatial and temporal coverage of the Mariner 6 and 7 infrared spectrometer (IRS), Mariner 9 infrared interferometer spectrometer (IRIS), and telescopic observations and by the limited spectral resolution of the Viking infrared thermal mapper (IRTM) instruments. Previous attempts to remove atmospheric effects have used ratios of different regions [*Pollack et al.*, 1990; *Roush et al.*, 1995; *Moersch et al.*, 1997]. The ratios may considerably reduce the atmospheric effects on the spectra, but the ratio remains a complicated mixture of two surface spectra. In addition, differences in atmospheric conditions, topography, and emission angles commonly introduce significant atmospheric artifacts in ratio spectra.

We report here on two algorithms that can successfully separate the atmospheric contribution to the observed radiance from the underlying surface emissivity spectrum. Although these two surface-atmosphere separation (SAS) algorithms have different philosophies and use very different mathematics, they yield very similar results. The first algorithm, which we will call the Radiative Transfer Algorithm, uses radiative transfer and successive least-squares fitting to find spectral shapes first for atmospheric dust, then for water-ice aerosols, and finally for surface emissivity. The second algorithm, which we will call the Deconvolution Algorithm, uses a combination of factor analysis, target transformation, and deconvolution to simultaneously find dust, water ice, and surface emissivity spectral shapes.

In the next section we describe the TES instrument and the characteristics of the data used in this study. In section 3 we describe the Radiative Transfer SAS Algorithm. In section 4 we describe the Deconvolution SAS Algorithm. In section 5 we present a discussion and comparison of results from the two SAS algorithms, and we provide a brief summary in section 6. It is not the purpose of this paper to perform an analysis of the surface emissivity spectra that we obtain. That analysis is presented in the accompanying paper by *Christensen et al.*, this issue (a).

2. Data Set

2.1. TES Instrument

The Thermal Emission Spectrometer (TES) is a thermal infrared spectrometer with additional broadband visible and thermal channels [*Christensen et al.*, 1992]. Six detectors in a three-by-two array simultaneously take spectra covering the spectral range from 200 to 1600 cm^{-1} (6–50 μm), with a selectable sampling of either 5 or 10 cm^{-1}. A pointing mirror allows TES to view from nadir to above both the forward and aft limbs. For daytime spectra taken over a warm (275 K) surface the signal-to-noise ratio in a single TES spectrum is 400:1 at 1000 cm^{-1} and better than 100:1 over the spectral range 200–1300 cm^{-1} [*Christensen*, 1999].

Included in the spectral range covered by the TES are features caused by CO_2 and water vapor gas, dust

and water-ice aerosols, and surface materials. The main CO_2 gas absorption is centered at 667 cm^{-1} (15 μm) although there are weaker, but important, CO_2 absorptions centered at 550, 790, 961, 1064, 1260, and 1366 cm^{-1} [*Maguire*, 1977]. Water vapor has absorptions at 200–400 cm^{-1} and at 1400–1800 cm^{-1} that can be seen in TES spectra. Dust aerosols have a broad peak centered at 1075 cm^{-1} and nonnegligible absorption throughout the entire spectrum. Water-ice aerosols have a broad peak near 825 cm^{-1}, a sharper peak at 229 cm^{-1}, and little absorption for wavenumbers > 1000 cm^{-1}. The most transparent part of the overall spectrum is near 1300 cm^{-1}.

2.2. Data Used in This Study

We report here on data taken during initial aerobraking (September 1997 to March 1998) and the "science phasing" period (March–September 1998). The primary requirement for producing a good surface emissivity spectrum is to have a warm surface (greater than ~250 K). High spatial resolution is also desirable to minimize the number of mixed surface components, as is relatively low atmospheric opacity. To obtain surface emissivity spectra, we therefore use daytime data taken near periapsis for an orbit during science phasing. Surface temperatures were sufficiently high, and atmospheric opacities were generally low [*Smith et al.*, this issue]. As a test of these algorithms, we also use data from an orbit acquired 4 months earlier during aerobraking which cover nearly the same longitude. To retrieve the spectral shapes of dust and water-ice aerosols, we have selected daytime, periapsis data where the contribution from dust or from ice dominates other atmospheric and surface features. Table 1 gives a complete listing of all the data used in this study.

3. Radiative Transfer Algorithm

The first algorithm we describe for the separation of surface and atmospheric spectral components is the Radiative Transfer Algorithm. It uses radiative transfer and successive least squares fitting to determine component spectral shapes and amplitudes. The TES radiance spectra are first converted to spectra of equivalent opacity by assuming all deviations from blackbody are caused by well-mixed, nonscattering atmospheric absorbers.

Candidate spectra are fit with dust and water-ice aerosol spectral shapes that are determined using carefully selected standard data sets (which are described in sections 3.2 and 3.3). *Bandfield et al.* [this issue] have demonstrated that except at the height of large dust storms when dust opacities approach unity, the spectral shapes of the dust and water-ice components are essentially constant for the TES data collected to date. When the residual in the fit is significantly above the expected noise, we infer that there is a third component contributing to the observed spectrum besides atmospheric dust and water-ice aerosols. The spectral shape of this third component is then solved for by finding the spectral shape that, along with the dust and ice spectral shapes which are held constant [*Bandfield et al.*, this issue], best fits the observed opacity spectrum. The resulting (surface) spectral shape is then transformed from opacity to emissivity.

3.1. Basic Equations and Assumptions

The first step in the Radiative Transfer Algorithm is to convert the observed radiance spectrum to an equivalent opacity spectrum. We accomplish this by using the method described by *Smith et al.* [this issue]. Neglecting the small contributions from the solar beam and scattering from atmospheric aerosols, and assuming a plane-parallel atmosphere, the observed monochromatic radiance as a function of wavenumber, $I_{obs}(\nu)$, of Mars can be written as

$$I_{obs}(\nu) = \epsilon(\nu)\ B[T_{surf}, \nu]\ e^{-\tau_0(\nu)/\mu} + \int_0^{\tau_0(\nu)} B[T(\tau), \nu]\ e^{-\tau/\mu}\ d\tau, \qquad (1)$$

where $\epsilon(\nu)$ is the surface emissivity at frequency ν, $\tau_0(\nu)$ is the normal column-integrated aerosol opacity, μ is the cosine of the emission angle, $B[T, \nu]$ is the Planck function, T_{surf} is the surface temperature, $T(\tau)$ is the atmospheric temperature profile, and the integral is performed from the spacecraft (at $\tau = 0$) to the surface (at τ_0).

For each spectrum to be studied, (1) is used to find equivalent opacity as a function of frequency. By assuming a well-mixed opacity source, the required atmospheric temperature profile $T(\tau)$ can be converted to $T(p)$, a quantity retrieved from the 15-μm CO_2 band as described by *Conrath et al.* [this issue]. The conversion from radiance to opacity allows the Radiative Transfer Algorithm to directly account for atmospheric conditions and allows for the quantitative retrieval of the relative opacities of atmospheric (and surface) contributions.

By working with opacity spectra, the final surface spectrum is obtained in terms of an "effective opacity" instead of emissivity as desired. Using the assumption that surface emissivities are not too different from unity, we can write

$$\tau(\nu) = \left(\frac{\partial \tau}{\partial \epsilon}\right)[1 - \epsilon(\nu)], \quad (2)$$

where $\epsilon(\nu)$ is surface emissivity and the derivative is also a function of frequency. The derivative term is computed numerically for each spectrum and averaged over all spectra being examined to find a single conversion from opacity to emissivity. The derivative term is generally near unity and has a smooth slope in frequency with higher absolute value at higher wavenumbers.

3.2. Dust Spectral Shape

We assume that the spectral opacity of each aerosol can be described in terms of a basic spectral shape $f(\nu)$ multiplied by a scaling factor A that varies from spectrum to spectrum. The next step in the Radiative Transfer Algorithm is to find the spectral shape of the atmospheric dust aerosols outside the 15-μm CO_2 band. Dust is the most prominent spectral feature in nearly every spectrum and is accounted for first. Figure 1 shows typical daytime spectra for three orbits (61, 93, and 112, at L_s= 234°, 256°, and 266°, respectively) over high-albedo areas in terms of equivalent brightness temperature. The data from all three of these orbits were taken over the Isidis Planitia region (see Table 1). Clearly evident in these spectra are the 15-μm (667-cm^{-1}) CO_2 band and a broad absorption from 800 to 1300 cm^{-1} caused by dust. Dust absorption exists at a lower level through the 15-μm CO_2 band and continues on the low wavenumber side of the CO_2 band.

These spectra have very little contribution either from water ice or from nonunit surface emissivity for several reasons. First, high-albedo surfaces such as Isidis Planitia have surface emissivity near unity in the wavelength regions studied [*Christensen*, 1982, 1998]. Second, this seasonal and local time period is one of relatively low water-ice cloud occurrence, and these spectra are from regions not known for significant water-ice cloud formation [*Christensen*, 1998; *Beish and Parker*, 1990; *Curran et al.*, 1973; Pearl et al., submitted manuscript, 1999].

To obtain the dust spectral shape, we average all the opacity spectra from a small spatial region. Approximately 100–200 spectra are used for each orbit. In a final step the contribution from four of the weak CO_2 absorptions (961, 1064, 1260, and 1366 cm^{-1}) are removed in a simple way by assuming that the true dust spectral shape varies smoothly through each CO_2 absorption and then performing a least squares fit of the known shape of the CO_2 bands to the data. Figure 2 shows the resulting dust spectral shapes. The spectral shape for each orbit has been normalized to unity at its maximum value. The three shapes are the same to our level of measurement uncertainty. We use only the data from 320 to 540 cm^{-1} and from 800 to 1350 cm^{-1} because of the increased noise and contribution from CO_2 and water vapor outside those regions. Water vapor has a number of weaker absorptions extending to frequencies up 500 cm^{-1} that we have not attempted to correct for. The exclusion between 540 and 800 cm^{-1} is because CO_2 is opaque in that spectral interval.

For the remainder of the discussion of the Radiative Transfer Algorithm we will assume that the dust spectral shape is given by the average of the three dust spectral shapes shown in Figure 2 and is the same everywhere. A constant dust spectral shape implies a constant dust composition and particle size distribution in a column-averaged sense through the atmosphere. Although this assumption may not be valid in the middle of the initiation of a large dust storm, *Bandfield et al.* [this issue] show that this approximation is good for all spectra collected to date with 9-μm dust opacities < 0.5.

3.3. Water-Ice Spectral Shape

The next step in the Radiative Transfer Algorithm is to find the spectral shape of atmospheric water-ice aerosols. Figure 3 shows typical spectra for three orbits (33, 55, and 132, at L_s=210°, 229°, and 276°, respectively) over Arsia Mons, one of the three Tharsis volcanos. Besides the CO_2 and dust features seen in Figure 1, a broad absorption caused by water-ice aerosols is clearly seen between 750 (at the edge of the CO_2 band) and 975 cm^{-1}.

We assume that the spectral shape of dust is already known and is fixed. Then, we obtain the spectral shape of water-ice aerosols by finding the one spectral shape that, along with the fixed dust spectral shape, best fits the observed opacity spectra. If n spectral points are to be fit and m spectra are to be used, then a least squares fit is performed over $n+2m$ variables. The first n variables describe the spectral

shape of water ice, and the remaining $2m$ variables describe the concentration or overall scaling of the dust and ice spectral shapes for each spectrum. We fit 100 spectral points and typically use approximately 50–100 averaged spectra.

The spectral shape that we obtain for water ice in this way is not unique. Any linear combination, $f'_{\rm ice}$, of our retrieved water-ice spectral shape and the fixed dust spectral shape will fit the observed opacities exactly as well as the the shape we originally found. The difference will be that the derived concentrations or opacities will be different for the two cases. Put another way, there is an unknown amount of mixing of the fixed dust spectral shape in our derived water-ice spectral shape. This unknown amount of mixing can be described by one single scalar value, α, which applies to all the spectra being considered.

$$f'_{\rm ice}(\nu) = \alpha f_{\rm dust}(\nu) + f_{\rm ice}(\nu) \tag{3}$$

We find this one extra parameter by imposing one additional constraint. For this constraint we assume that there is no correlation between small-scale variations in dust and water-ice opacities.

Our data come from the periapsis pass of an orbit, and we therefore have narrow strips of data running nearly north-south. To allow dust and water ice to both have large-scale trends (that can be physically or accidentally correlated), we impose the above constraint of noncorrelation by requiring that the derivatives of opacity, $A'(\text{lat}, \text{lon})$, with latitude be uncorrelated:

$$\sum_{\text{spectra}} \left(\frac{\partial A'_{\rm dust}(\text{lat}, \text{lon})}{\partial \text{lat}} \right) \left(\frac{\partial A'_{\rm ice}(\text{lat}, \text{lon})}{\partial \text{lat}} \right) = 0. \tag{4}$$

Thus the constraint of noncorrelation applies only to small-scale spectrum-to-spectrum variations in dust and water-ice opacity, not to larger regional-scale gradients.

The dust and water-ice opacities $A'_{\rm dust,ice}$ are functions of the single mixing coefficient, α, in (3). Once a value for the mixing coefficient, α, is found that satisfies (4), the true water-ice spectral shape can be computed using (3). As with the dust spectral shape, the four weak CO_2 absorptions at 961, 1064, 1260, and 1366 cm^{-1} are fit for and removed, and the water-ice spectral shape is normalized to unity at its greatest amplitude (which occurs at 825 cm^{-1}) as a final step.

Figure 4 shows the retrieved spectral shapes for water ice. As was the case with dust, the ice spectral shapes are quite similar for the three orbits. For the remainder of the discussion we will assume that the ice spectral shape is fixed and is given by the average of the three spectral shapes shown in Figure 4.

3.4. Surface Temperature Ambiguity

The negative values in the spectral shapes in Figure 4 immediately call into question the physical meaning of these spectral shapes. The reason for the negative values is that there is an ambiguity in the determination of surface temperature. To perform the radiative transfer necessary to derive an opacity spectrum we must first adopt a surface temperature. The most transparent part of the spectrum is at around 1300 cm^{-1}, so we use the brightness temperature in a small spectral window near that frequency (1285–1315 cm^{-1}) as an estimate of surface temperature. This means that by definition in (1), opacity is zero there.

We assume that for a given spectrum, opacity $\tau(\nu)$ has the form:

$$\tau(\nu) = A_{\rm dust}(\text{lat}, \text{lon}) f_{\rm dust}(\nu) + A_{\rm ice}(\text{lat}, \text{lon}) f_{\rm ice}(\nu), \tag{5}$$

where the $f(\nu)$ functions are the spectral shapes that we have been deriving and the $A(\text{lat}, \text{lon})$ parameters describe the spectrum-to-spectrum opacity variation of dust and water-ice aerosols.

However, if there is a nonzero opacity at 1300 cm^{-1}, then there will be an error $\Delta T_{\rm surf}$ in our surface temperature. In opacity the error is

$$\tau'(\nu) = \Delta T_{\rm surf} \frac{\partial \tau(\nu)}{\partial T_{\rm surf}}. \tag{6}$$

This is a third term that we can add to (5). We can combine the second (water-ice) term and the opacity error term as

$$A_{\rm ice}(\text{lat}, \text{lon}) \left[f_{\rm ice}(\nu) + \left(\frac{\Delta T_{surf}}{A_{\rm ice}(\text{lat}, \text{lon})} \right) \frac{\partial \tau(\nu)}{\partial T_{\rm surf}} \right]. \tag{7}$$

Therefore the actual spectral shape can be the derived shape plus any constant times $\partial\tau(\nu)/\partial T_{\rm surf}$. In the case of the water-ice spectral shape, there must be a non zero opacity at 1300 cm^{-1} and hence an error in surface temperature $T'_{\rm surf} = \text{constant} \times A_{\rm ice}$. The surface temperature error required to bring all of the

spectral shape curves above zero (and therefore be physical) is typically less than or about 1–2 K for all but the most extreme icy spectra.

This same surface temperature ambiguity exists for the dust spectral shape as well and will also exist when we derive a surface emissivity spectral shape. However, the error is probably very small for dust because the spectral shape is everywhere positive. This surface temperature ambiguity does not affect the mathematics of separating the water-ice feature from observed opacity spectra.

3.5. Search for Spectra Not Well Fit By Dust and Ice

Figure 5 shows the relative opacities of dust and water-ice aerosols along the orbit 55 periapsis pass. These opacities are obtained for each spectrum by performing a least squares minimization to find the best fitting scaling factors (opacities) given the previously retrieved (and fixed) dust and water-ice spectral shapes. Recalling (5), $f_{\text{dust}}(\nu)$ and $f_{\text{ice}}(\nu)$ are known and fixed. We solve for $A_{\text{dust}}(\text{lat}, \text{lon})$ and $A_{\text{ice}}(\text{lat}, \text{lon})$. Therefore the dust opacity shown represents the opacity at the dust absorption maximum (1075 cm^{-1}), where the spectral shape has unit amplitude. Likewise, the water-ice opacity represents the opacity of water ice at 825 cm^{-1}.

The profile of dust opacity closely follows the inverse of topography over the flank of Arsia Mons in Figure 5. There are at least two large discrete ice clouds apparent near the summit and on the southern flank of Arsia Mons. The residual opacity shown in Figure 5 is the mean absolute difference over the entire spectrum between the opacity retrieved from the observations and the opacity given by the fit. Therefore the observed opacity spectra can be described by dust and water ice alone to the level of about 0.01–0.02 opacity averaged over the spectrum. This residual value indicates that to the level of the noise in the data there is no surface emissivity contribution at this location in these spectral regions.

Dust and water-ice opacities and the residual values are given in Figure 6 for orbit 219 (L_s=305°). Here there are variable amounts of dust, and there is significant structure in the profile of water-ice opacity. North of 20°N latitude, the residual is relatively high, but it is noisy and rises in a systematic manner consistent with the colder temperatures (and noisier data) to the north. However, between about 15° and 35°S latitude there is a well-defined area with high residual that is not caused by increased noise. Surface temperatures are high, and the structure and rise of the residual from about 0.01 to over 0.03 are much higher than the peak-to-peak variability in the residual. Further examination shows that this rise in residual is very closely correlated with the low-albedo region Terra Cimmeria. It must be concluded that in this region the derived spectral shapes of dust and water ice alone do not accurately describe the observed spectral shape of opacity and that there is an additional surface emissivity component contributing to the observed spectrum.

3.6. Surface Emissivity Spectral Shape

We proceed to find the surface spectral shape in much the same way as we did when we found the water-ice spectral shape. Now we assume that the spectral shapes of both dust and water ice are already known and are fixed. A surface spectral shape is obtained by finding a single additional spectral shape that, along with the fixed dust and water-ice spectral shapes, best fits the observed opacity spectra. If n spectral points are to be fit and m spectra are to be used, then a least squares fit is performed over $n+3m$ variables. As before, the first n variables describe the spectral shape of the surface and the remaining $3m$ variables describe the concentration or overall scaling of the dust, water ice, and surface spectral shapes for each spectrum.

The problem of the mixing of spectral shapes is again present, and this time both the dust and the ice spectral shapes can mix into the surface spectral shape, giving a new surface shape $f'_{\text{surf}}(\nu)$ with exactly as good a fit:

$$f'_{\text{surf}}(\nu) = \beta_1 f_{\text{dust}}(\nu) + \beta_2 f_{\text{ice}}(\nu) + f_{\text{surf}}(\nu). \quad (8)$$

Because there are two scalar mixing coefficients, β_1 and β_2, two additional constraints are required. Following the example of the derivation of the water-ice spectral shape, the constraints chosen were that there be no correlations between the latitude derivative of surface effective opacity and either dust or ice opacity:

$$\sum_{\text{spectra}} \left(\frac{\partial A'_{\text{surf}}(\text{lat}, \text{lon})}{\partial \text{lat}} \right) \left(\frac{\partial A'_{\text{dust}}(\text{lat}, \text{lon})}{\partial \text{lat}} \right) = 0 \quad (9a)$$

$$\sum_{\text{spectra}} \left(\frac{\partial A'_{\text{surf}}(\text{lat}, \text{lon})}{\partial \text{lat}} \right) \left(\frac{\partial A'_{\text{ice}}(\text{lat}, \text{lon})}{\partial \text{lat}} \right) = 0. \quad (9b)$$

The concentrations $A'(\mathrm{lat}, \mathrm{lon})$ are functions of the mixing coefficients, $\beta_{1,2}$, so the above pair of equations can be solved for $\beta_{1,2}$. The true surface effective opacity shape, $f'_{\mathrm{surf}}(\nu)$, can then be obtained from (8), and the four weak CO_2 absorptions at 961, 1064, 1260, and 1366 cm^{-1} are fit for and removed.

The final step is to convert the surface effective opacity spectrum into a surface emissivity spectrum. We first define a new function, $g_{\mathrm{surf}}(\nu)$, which is the surface spectral shape given in terms of emissivity:

$$g_{\mathrm{surf}}(\nu) = f'_{\mathrm{surf}}(\nu)\tau(\nu)\left(\frac{\partial\epsilon(\nu)}{\partial\tau(\nu)}\right). \qquad (10)$$

Then, using (2), the surface emissivity $\epsilon(\nu)$ at a given location is given by

$$\epsilon(\nu) = 1 - A_{\mathrm{surf}}(\mathrm{lat}, \mathrm{lon})g_{\mathrm{surf}}(\nu), \qquad (11)$$

where A_{surf} is a parameter that describes the spectrum-to-spectrum variation in the strength of the surface emissivity feature. As stated earlier, the derivative is computed for each spectrum and summed to form an average conversion function.

Figure 7 shows the surface emissivity spectral shape for orbit 219. As with the dust and ice shapes, there is a surface temperature ambiguity here too. However, because the spectral shape is positive very nearly everywhere, we believe that the surface temperature error for this spectrum is small (< 0.5 K). However, we cannot rule out that there is some component (constant $\times\ \partial\epsilon(\nu)/\partial T_{\mathrm{surf}}$) missing.

Figure 8 shows the same quantities as Figure 6 (opacities and residual for orbit 219) except that the surface spectral shape shown in Figure 7 (converted back to effective opacity) has been included in the spectrum-by-spectrum fit for opacity. The region where a nonunit surface emissivity is required to accurately reproduce the observed opacity spectra is clearly seen from 15° to 35°S latitude. The slight nonzero surface contribution north of 15°S latitude is at or below the level of the residual and so can be considered to be consistent with zero. Notice that the dust opacity values (and to a lesser extent the water-ice opacity values as well) are significantly lower in the region where the surface contributes. This is because the spectral shape of the surface emissivity is broadly similar to that of dust. This underscores the fact that a full treatment of the analysis of a TES spectrum requires consideration of both atmospheric and surface features.

3.7. Discussion of Uncertainties

A number of steps must be performed in order to obtain the surface spectral shape shown in Figure 7, and uncertainty in the final spectrum is potentially introduced at every step. First, the combination of instrument noise in the original radiance spectra, calibration uncertainties, and uncertainty in the retrieval of atmospheric temperatures leads to a probable error in the derived opacity spectra of as much as 0.05 (see the discussion of opacity uncertainties by *Smith et al.* [this issue]). However, because we are primarily interested in spectral shapes (not the overall scaling), and we typically use of the order of 100 spectra in finding the spectral shapes, these are a minor source of uncertainty in our spectral shapes. The level of these errors is indicated in the variation in the three dust spectral shapes (Figure 2) derived from different orbits and is $< 2\%$ of the maximum amplitude of the spectral shape.

Of greater concern is the uncertainty in the estimation of mixing coefficients. Although well-defined for a particular set of data, the assumption that opacities must have zero correlation is ad hoc, and changing the limits of the data set can change the mixing constants in (3) and (8). Experience shows that differences of up to 10–20% in the mixing coefficients are possible without significantly adding large correlations between opacities. This means that up to 10–20% of the dust or water-ice spectral shape could be added or removed from the derived surface spectral shape. Evidence of this can be seen in the water-ice spectral shape (Figure 4), which shows variations of 5–7% where the dust spectral shape is largest (near 1000–1150 cm^{-1}).

One empirical measure of the amount of uncertainty in the surface emissivity spectral shape is to derive the surface emissivity spectral shape for each of the six TES detectors separately. Figure 9 shows the results. As expected, a difference in mixing coefficients (especially the water-ice mixing coefficient from detector 6) produces uncertainties of up to about 10% in the final spectral shape. Notice that uncertainties in the mixing coefficients tend to introduce primarily large-scale slopes since the spectral shapes of dust and water ice are both relatively smooth. Therefore this exercise primarily gives information on the reliability and repeatability of small-scale (< 100-cm^{-1}) features. This point is addressed again in section 5.1 when results from the Radiative Transfer Algorithm are compared to those of the following section.

Figur

4. Factor Analysis and Deconvolution Algorithm

The Deconvolution Algorithm is an alternative SAS algorithm that attempts to fit the measured TES apparent emissivity spectrum in a linear least squares manner by using both atmospheric spectral shapes and mineral spectral shapes simultaneously. The derived weights of the atmospheric components are removed from the original TES spectrum to obtain the surface spectral signature. The derived weights of the mineral components may be normalized to estimate surface mineralogical composition.

While atmospheric spectral properties are generally nonlinear, *Bandfield et al.* [this issue] have demonstrated that warm daytime TES spectra may be very closely approximated using linear combinations of atmospheric spectral shapes. The high temperature contrast between the Martian surface and atmosphere, and the limited range of surface temperature (~260–290 K) used in this analysis, allows this linear approximation to be accurate. The assumptions and validity of a linear surface-atmosphere separation will be described and addressed here. We show here that the TES spectra can be fit with both atmospheric and mineralogical spectral components simultaneously to separate surface and atmospheric signatures and to obtain atmospheric and mineralogical concentrations.

4.1. Derived Atmospheric Shapes From Target Transformation

Determining the spectral shape of the atmospheric components present in the TES spectra is necessary for the accurate separation of atmospheric components from any surface signature present. *Bandfield et al.* [this issue] have successfully isolated the spectral shapes of both water-ice clouds and atmospheric dust. Isolation of these shapes over a variety of data subsets has established that the water-ice and atmospheric dust spectral shapes remain constant with the exception of the relative depth of CO_2 hot bands and water vapor bands and slight variations in the water ice.

In nearly all conditions the dust signature is present in a high enough concentration that the dust spectral shape can be derived by using spectra from the orbit and local area of interest. Using a locally derived dust spectrum in the technique presented here ensures the accuracy of the weight and shape of CO_2 hot bands and water vapor relative to the atmospheric dust. If a locally derived dust shape is unavailable, then it is also possible to use several dust shapes from other regions and orbits because most of the shape variation may be accounted for with just two atmospheric dust shapes with different atmospheric opacities.

The water-ice spectral shape is usually present at a lower amplitude than the dust in the TES spectra. However, its presence is nearly ubiquitous in the TES aerobraking and science phasing orbit (SPO) data, and it is important to separate its signature from the surface spectrum for an accurate interpretation. If water ice is present only at low levels (825-cm^{-1} opacity less than ~0.05), then the isolated water-ice spectral shape is often noisy. As a result, two water-ice spectral shapes that were isolated from orbits with a high water-ice concentration are used in the Deconvolution Algorithm. These two shapes cover the small range of water-ice spectral shapes recovered to date [*Bandfield et al.*, this issue], which is likely caused by differences in the particle size distribution. Experience shows that using a locally derived ice shape is not necessary to produce an accurate separation of the water-ice contribution because the range of water-ice spectral shapes is not great and the contribution of water ice to the shape of the measured spectrum is almost always much lower than that of the atmospheric dust.

4.2. Spectral Library

In addition to having accurate atmospheric spectral shapes, it is also important to include as many mineral spectral components as possible to model the surface. Sixty rock-forming mineral spectra were selected from the Arizona State University Spectral Library [*Christensen et al.*, this issue (b)] for use in the Deconvolution Algorithm. The mineral spectra selected cover a wide variety of mineral classes, including carbonates, sulfates, oxides, and silicates.

4.3. Deconvolution Algorithm

The Deconvolution Algorithm provides a least squares fit to the measured spectrum by using a linear combination of atmospheric and mineral spectral shapes. This algorithm has been used with excellent results in determining a wide variety of rock compositions and mineralogies [*Ruff*, 1997; *Hamilton*, this issue; *Feely and Christensen*, 1999] from laboratory spectra. The procedure for performing the least squares fit is modeled after that of *Ramsey and Christensen* [1998] with a slight modification that removes a constraint that forces component sums closer to unity.

Because a negative concentration for a particular mineral is a possible solution to a least squares fit, the Deconvolution Algorithm uses an iterative approach that removes all components with negative concentrations from the set of spectral shapes being fit. The fitting is then repeated with the remaining spectral shapes until only positive component concentrations are derived. The same fitting procedure is then performed again using all minerals similar in composition to those remaining in the final iteration. For example, if the final iteration contains positive concentrations of only diopside and andesine, then the algorithm is run again with a set of spectral shapes that includes all feldspars and clinopyroxenes that are spectrally similar to andesine and diopside but excludes all other mineral spectra. This additional step reduces the possibility that a correct mineral is accidentally removed in the iterative process.

4.4. Assumptions and Approximations

This Deconvolution Algorithm makes two basic assumptions: (1) The measured apparent emissivity spectrum can be modeled by using a linear combination of atmospheric and surface spectral shapes; this assumes that surface spectra can be described using a linear combination of individual mineral spectra and that the spectral contribution of the atmosphere may also be reproduced using a linear combination of atmospheric components. (2) All atmospheric and surface spectral components in the measured TES spectrum are accounted for in the set of spectral shapes used for the least squares fit.

It has been well established that thermal infrared spectra of surfaces composed of multiple minerals may be modeled by using linear combinations of each mineral spectrum weighted by the areal fraction of the surface measured [*Lyon*, 1965; *Thomson and Salisbury*, 1993; *Ramsey and Christensen*, 1998]. Several studies [*Gillespie*, 1992; *Ramsey and Christensen*, 1998; *Feely and Christensen*, 1999; *Hamilton*, this issue] have used this property to demonstrate that mineralogical information may be retrieved from a mixed spectrum by performing a least squares fit using a mineral spectral library. The calculated concentration of each mineral spectral component represents the areal fraction of the surface composed of each mineral. Concentration errors have been estimated to be ~5–15%. For this study, error in surface mineralogy is estimated to be ~15–20% because of lower spectral resolution and a more limited spectral range used in this study as well as the influence of the atmosphere on TES spectra.

The Deconvolution Algorithm takes advantage of the results of *Bandfield et al.* [this issue] that indicate that the TES apparent emissivity spectra may be closely modeled by using linear combinations of atmospheric and surface spectral components. The factor analysis and target transformation methods described by *Bandfield et al.* [this issue] indicate that warm, daytime TES emissivity spectra of uniform, high-albedo regions may be modeled closely (within 0.010 RMS in all spectra over a region of high water-ice cloud, dust, and topographic variability) by using only three components which can be accurately isolated from the set of mixed spectra: atmospheric dust, water-ice cloud, and blackbody spectral shapes. When the factor analysis is performed by using low-albedo region spectra, an additional component is detected and is required to model the TES spectra.

A basic assumption in factor analysis as it is applied here is that each spectrum is a linear combination of its components. Subpixel spectral mixing of surface composition has been demonstrated to be linear in the thermal infrared, but the combination of emission (surface) and transmission (atmosphere) components in the spectra is more complex, and the linearity of varying emissivity components combined with varying transmission components must be considered.

The linear mixing of the surface materials in emission is given by

$$\sum_{i=1}^{n} c_i \mathbf{e}_i = \mathbf{d} \tag{12}$$

and

$$\sum_{i=1}^{n} c_i = 1 \tag{13}$$

where c_i is the areal concentration of each of the n components, $\mathbf{e}_i$ is the emissivity spectrum of each of the components, and $\mathbf{d}$ is the measured spectrum. When observing a surface through an absorbing atmosphere that contains materials of transmissivity $\mathbf{t}_{1,\ldots,m}$, the resultant measured value is

$$\left(\sum_{i=1}^{n} c_i \mathbf{e}_i\right) \cdot \left(\sum_{j=1}^{m} a_j \mathbf{t}_j\right) = \mathbf{d}, \tag{14}$$

where a_j represents the concentration of each atmospheric component, $\mathbf{t}_j$. In this form the measured

spectrum is the surface emissivity multiplied by the transmissivity of the atmosphere. Here scattering and reemission by atmospheric aerosols are neglected since the opacity of dust and water ice is generally considerably less than unity [*Smith et al.*, this issue], and surface temperature is much greater than the atmospheric temperature. The system is not linear in this form, and the original components cannot be obtained through linear, least squares deconvolution. However, an approximation may be made for (14) using the following relation:

$$\mathbf{x} \cdot \mathbf{y} = \alpha\mathbf{x} + \beta\mathbf{y} + \gamma\mathbf{i}. \quad (15)$$

In this equation, $\mathbf{x}$ and $\mathbf{y}$ are the emissivity and transmissivity spectra being multiplied, $\mathbf{i}$ is a blackbody spectrum, and α, β, and γ are constants. This approximation may be made because natural surface emissivities are commonly close to unity (greater than ~0.90) and atmospheric opacities are low (opacity less than ~0.3 at 1075 cm^{-1}). Under these conditions a typical basalt emissivity spectrum may be modeled using the approximation given by (15) to within 0.0030 (RMS error between actual and modeled spectra is 0.0009) at all wavelengths (Figure 10).

When (14) is rearranged using the relation from (15), the following is obtained:

$$\alpha\left(\sum_{i=1}^{n} c_i\mathbf{e}_i\right) + \beta\left(\sum_{j=1}^{m} a_j\mathbf{t}_j\right) + \gamma\mathbf{i} = \mathbf{d}, \quad (16)$$

which can be expanded and rewritten as

$$(\alpha c_1\mathbf{e}_1 + \alpha c_2\mathbf{e}_2 + \cdots + \alpha c_n\mathbf{e}_n) + (\beta a_1\mathbf{t}_1 + \beta a_2\mathbf{t}_2 + \cdots + \beta a_m\mathbf{t}_m) + \gamma\mathbf{i} = \mathbf{d}. \quad (17)$$

As a result, a combination of emission from mixed surfaces and transmission through varying concentrations of atmospheric components can be expressed as a linear system of equations. Because the original factors have been multiplied by additional constants, the concentrations derived from a deconvolution of the measured spectrum will not be correct, but the surface areal concentration of a component may be recovered by

$$c_i = \frac{\alpha c_i}{\sum_{i=1}^{n} \alpha c_i}. \quad (18)$$

Recovery and identification are not limited to surface spectral components. Atmospheric components are also mixing in the same linear fashion and may be recovered as well.

4.5. Results

As a preliminary application of this technique, atmospheric dust and water-ice spectral shapes were isolated from a subset of orbit 219 data (Table 1) by using the method of *Bandfield et al.* [this issue]. This data subset shows low atmospheric dust and ice opacities and warm surface temperatures (~275 K) and covers both high- and low-albedo regions. An average of 78 spectra covering a spectrally uniform area of low albedo (Lambert albedo=0.12) were chosen for the atmospheric removal. This region was chosen for the initial application of this technique because low-albedo regions have been found to have strong emissivity spectral features [*Christensen*, 1982, 1998] and they have a high thermal inertia (inertia = 6–8 10^{-3} cal cm^{-2} $s^{-1/2}$ K^{-1}) [*Kieffer et al.* 1977; *Palluconi and Kieffer*, 1981], which indicates the material on the surface is dominated by particles > 300μm [*Presley and Christensen*, 1997]. Multiple scattering and volume scattering effects become prominent in spectra of surfaces with particle sizes less than ~100 μm [e.g., *Hunt and Vincent*, 1968; *Hapke*, 1981; *Salisbury et al.*, 1987; *Moersch and Christensen*, 1995]. Larger particle size mixtures and rocks may be modeled by using spectra of coarse grained (710 to 1000-μm) minerals [*Ramsey and Christensen*, 1998; *Feely and Christensen*, 1999; *Hamilton*, this issue], as in this application.

The Deconvolution Algorithm uses the spectral intervals 233–529 cm^{-1} and 794–1301 cm^{-1}. The measured spectrum was fit by using the isolated dust and water-ice spectral shapes (Figure 11) that were isolated by using the method of *Bandfield et al.* [this issue] together with the suite of mineral spectra. The fit was performed at wavenumbers > 400 cm^{-1} because of the limited wavelength range of the reference mineral spectra. However, as both the water ice and dust are derived from the TES data themselves, the surface spectrum could be recovered to 233 cm^{-1}. The deconvolution modeled the orbit 219 spectrum quite well (Figure 12) with an RMS error between measured and modeled spectra of 0.00232.

The derived concentrations of the atmospheric components were removed from both the measured and modeled spectra to produce atmosphere-corrected TES and modeled surface emissivity spectra (Figure 13). The resulting surface spectrum contains broad, shallow absorptions at both ~1000 and 400 cm^{-1} and is

Figure

Figure

Figur

well modeled by derived mineral components. There is no indication of residual water vapor, CO_2, or water ice in the surface spectrum. The surface spectrum does contain broad absorptions that are somewhat similar to the atmospheric dust, as they are both indicative of silicate materials. However, there are several important distinctions: (1) The ratio of the 400- to 1000-cm^{-1} absorption depth is greater in the derived surface spectra; (2) the atmospheric dust has a positive slope with increasing wavelength from 300 to 500 cm^{-1}, while the surface spectra contain a negative slope; and (3) the absorption near 1000 cm^{-1} of the surface spectra is more rounded or slightly square than the atmospheric dust absorption, which is more V-shaped. In addition to providing a surface spectral shape, this method also provides modal mineralogies which are discussed in an accompanying paper [*Christensen et al.*, this issue (a)].

5. Discussion

5.1. Differences Between the Two SAS Algorithms

The two algorithms presented here for the separation of atmospheric from surface emissivity spectral features differ in several key ways. The first is in the data used by the algorithms. The Radiative Transfer Algorithm incorporates radiative transfer by using equivalent opacity spectra. This is the natural quantity to use when dealing with atmospheric contributions to the spectrum but is somewhat awkward for describing the surface emissivity. The Deconvolution Algorithm uses equivalent emissivity spectra as its starting point. This is the natural quantity to use when describing the surface, but it cannot, in general, give accurate quantitative abundances for atmospheric absorptions. Because of the mixed nature of the problem, it is not immediately obvious which data set is preferable, although using opacity does allow for a more quantitative evaluation of component contributions.

The second major difference is in the computation of spectral shapes. The Radiative Transfer Algorithm uses a bootstrapping method of first finding the dust spectral shape, then the water-ice spectral shape, and, finally, the surface emissivity shape. Each of the previous shapes must be known before continuing to the next step, and dust and water-ice spectral shapes determined from outside the area of interest are used to find the surface emissivity spectral shape. On the other hand, the combination of factor analysis and the Deconvolution Algorithm can derive all three spectral shapes (dust, water ice, and surface emissivity) locally from one set of data. This advantage of the Deconvolution Algorithm is lessened by the fact that the dust and water-ice spectral shapes vary very little [*Bandfield et al.*, this issue].

A third difference is in the determination of a surface emissivity spectral shape. The Radiative Transfer Algorithm performs a completely unconstrained fitting for the spectral shape which must then be corrected using mixing coefficients for dust and water-ice spectral shapes determined in a separate step. The Deconvolution Algorithm performs a constrained fitting by using a spectral library of mineral spectral shapes. This avoids the extra step and associated uncertainties of finding mixing coefficients that the Radiative Transfer Algorithm has by allowing only spectral shapes that are linear combinations of spectra in the mineral library. However, this advantage is also a drawback since the Deconvolution Algorithm cannot produce the spectra of components that are not in the spectral library as the Radiative Transfer Algorithm can.

Finally, the Deconvolution Algorithm can also be applied to find surface emissivity spectra on a spectrum-by-spectrum basis (using dust and water-ice spectral shapes taken from a larger set of spectra), while the Radiative Transfer Algorithm requires at least a few dozen spectra to get a meaningful surface emissivity spectral shape and mixing coefficients.

5.2. Comparison of Surface Emissivity Spectral Shapes

The two SAS algorithms described above are quite different in their approach, yet the results are very similar. Plate 1 shows a comparison of the surface emissivity spectral shapes obtained from the Radiative Transfer and the Deconvolution SAS Algorithms. Results are shown for orbits 56 ($L_s = 230°$) and 219 ($L_s = 305°$) which are within approximately 2° in longitude of each other. Approximately the same latitude range is covered by the data subsets from each orbit. The atmospheric conditions between orbit 56 and 219 are fairly different with orbit 56 having twice the dust opacity of orbit 219. Orbit 56 was soon after the height of the Noachis dust storm [see *Smith et al.*, this issue], and while this region (Terra Cimmeria) is on the opposite side of Mars from where the core of the dust storm was located, there was elevated dust opacity in Terra Cimmeria (9-μm opacity of 0.33) as well as a marked decline in the amount of water-ice

clouds compared with orbit 219 [*Pearl et al.*, submitted manuscript, 1999].

The curves in Plate 1 actually show two different comparisons. One is a comparison of results for different orbits over the same location (orbit 56 versus 219), and the other is a comparison of the two SAS algorithms (Radiative Transfer versus Deconvolution). Comparison of results from the two different orbits gives an indication of the precision with which each algorithm can obtain a surface emissivity spectral shape. Comparison of results from the two SAS algorithms gives an indication of the absolute accuracy of the spectral shapes. Despite the differences between atmospheric conditions during the two orbits and the differences between the numerical approaches of the two SAS algorithms, the agreement between all the spectra shown in Plate 1 is very good. The difference between results for orbits 56 and 219 for each algorithm is less than 5% of the overall amplitude of the spectral shape, and the difference between the two SAS algorithms is everywhere less than 20% of the overall amplitude. As before, the smaller-scale ($< 100\text{-cm}^{-1}$) spectral features are generally very reproducible between the spectra. Interpretation of these spectra is beyond the scope of this paper. *Christensen et al.* [this issue (a)] examine the mineralogic implications of these surface emissivity spectra in an accompanying paper.

The difference between results for orbits 56 and 219 from the Radiative Transfer Algorithm (black and blue lines in Plate 1) is very close to the spectral shape of water ice. In this case, although the mixing coefficient for dust has been accurately determined, the mixing coefficient for water ice appears to be in error by ~20%. The retrieved water-ice opacity is noiselike and < 0.01 and is consistent with there being no water ice present at all at this time and place. Therefore, the mixing coefficient for water ice is not well constrained. This difficulty can be overcome by holding water-ice opacity to zero when fitting for the surface spectral shape. Then, the water-ice mixing coefficient must be zero and need not be computed. The fifth (purple) line in Plate 1 shows the surface spectral shape computed by using the Radiative Transfer Algorithm and assuming water-ice opacity to be zero. The agreement with the surface spectral shapes from orbit 219 and with those obtained from the Deconvolution Algorithm is noticeably better.

5.3. Comparison of Dust and Water-Ice Spectral Shapes

Figur

Figure 14 shows a comparison of dust and water-ice spectral shapes obtained by the Radiative Transfer and the Deconvolution Algorithms. The spectral shapes from the Radiative Transfer Algorithm are those shown in Figures 2 and 4. The spectral shapes from the Deconvolution Algorithm have been linearly rescaled to match the depths of the spectral shapes from the Radiative Transfer Algorithm. The agreement is quite good, considering the differences in the two algorithms. The difference in the dust spectral shape between 1025 and 1100 cm^{-1} is caused by the inclusion of the CO_2 hot bands in the spectral shape derived in the Deconvolution Algorithm, whereas these were separately removed in the Radiative Transfer Algorithm. The amplitude offset in the dust spectral shapes at 300–575 cm^{-1} is caused by the difference between expressing the spectral shape in terms of opacity and expressing the spectral shape in terms of emissivity. The derivative $\partial\tau/\partial\epsilon$ in (2) is a function of frequency, and so the amplitude of an emissivity representation cannot be matched to an opacity representation everywhere by a linear scaling. The small difference between the two water-ice spectral shapes at 300–575 cm^{-1} is again consistent with the difference between an opacity and an emissivity representation.

6. Summary

We have presented two algorithms that can successfully separate the contribution of atmospheric and surface emissivity spectral features from TES spectra taken in the nadir-viewing geometry. Each algorithm has advantages and disadvantages. We do not make a recommendation of one algorithm over the other here. We prefer to use both algorithms in parallel to check results against each other. We feel that this gives the maximum likelihood of obtaining a realistic and accurate surface emissivity spectrum.

The two surface-atmosphere separation (SAS) algorithms have been used to find spectral shapes for atmospheric dust and water-ice aerosols and for surface emissivity for several orbits. The results from the two algorithms are in good agreement. The process of producing a surface emissivity spectrum from the TES data is difficult, and interpretation of the spectra must be performed with care. However, we feel that it is feasible to produce surface emissivity spectra using the two algorithms described in this paper

and that the results are of sufficient quality that mineralogic interpretation is possible. Separation of the atmospheric and surface contributions to a TES spectrum is also very important for proper understanding of dust and water-ice aerosol opacity and spectral shape. In particular, dust opacities can be significantly overestimated if the nonunit surface emissivity is not accounted for.

During the mapping phase of the Mars Global Surveyor mission it will be possible to take advantage of limb-geometry observations and emission angle sequences to improve upon these techniques. However, when only nadir-geometry observations are available, as is the case for the large majority of the TES data taken during aerobraking and science phasing orbit, the algorithms presented here will produce reliable surface emissivity spectra.

Acknowledgments. The authors wish to thank Monte Kaelberer, Karen Horrocks, Eric Winter, and Emily Greene for providing software development and data-handling expertise at Goddard Space Flight Center. We also thank the TES operations team at Arizona State University, including Kelly Bender, Noel Gorelick, and Greg Mehall. Barney Conrath, Hugh Kieffer, John Pearl, Tim Titus, Ted Roush, Laurel Kirkland, and an anonymous referee provided helpful comments on this manuscript. Finally, we thank the entire spacecraft and mission operations teams at Jet Propulsion Lab and Lockheed Martin.

References

Bandfield, J. L., P. R. Christensen, and M. D. Smith, Spectral data set factor analysis and end-member recovery: Application to analysis of Martian atmospheric particulates, *J. Geophys. Res.*, this issue.

Beish, J. D., and D. C. Parker, Meteorological survey of Mars, 1969–1984. *J. Geophys. Res., 95*, 14,657–14,675, 1990.

Christensen, P. R., Martian dust mantling and surface composition: Interpretation of thermophysical properties, *J. Geophys. Res., 87*, 9985–9998, 1982.

Christensen, P. R., Variations in Martian surface composition and cloud occurrence determined from thermal infrared spectroscopy: Analysis of Viking and Mariner 9 data, *J. Geophys. Res., 103*, 1733–1746, 1998.

Christensen, P. R., Calibration report for the Thermal Emission Spectrometer (TES) for the Mars Global Surveyor Mission, Mars Global Surveyor Project, Jet Propul. Lab., Pasadena, Calif., 1999.

Christensen, P. R., et al., Thermal Emission Spectrometer Experiment: Mars Observer Mission, *J. Geophys. Res., 97*, 7719–7734, 1992.

Christensen, et al., Results from the Mars Global Surveyor Thermal Emission Spectrometer, *Science, 279*, 1692–1698, 1998.

Christensen, P. R., J. L. Bandfield, M. D. Smith, and V. E. Hamilton, Identification of a basaltic component on the Martian surface from Thermal Emission Spectrometer data, *J. Geophys. Res.*, this issue (a).

Christensen, P. R., J. L. Bandfield, V. E. Hamilton, D. A. Howard, M. D. Lane, J. L. Piatek, S. W. Ruff, and W. L. Stefanov, A thermal emission spectral library of rock-forming minerals, *J. Geophys. Res.*, this issue (b).

Conrath, B. J., J. C. Pearl, M. D. Smith, W. C. Maguire, S. Dason, M. S. Kaelberer, and P. R. Christensen, Mars Global Surveyor Thermal Emission Spectrometer (TES) observations: Atmospheric temperatures during aerobraking and science phasing, *J. Geophys. Res.*, this issue.

Curran, R. J., B. J. Conrath, R. A. Hanel, V. G. Kunde, and J. C. Pearl, Mars: Mariner 9 spectroscopic evidence for H_2O ice clouds, *Science, 182*, 381–383, 1973.

Feely, K. C., and P. R. Christensen, Quantitative compositional analysis using thermal emission spectroscopy: Application to igneous and metamorphic rocks, *J. Geophys. Res.*, this issue.

Gillespie, A. R., Spectral mixture analysis of multispectral thermal infrared images, *Remote Sens. Environ., 42*, 137–145, 1992.

Hamilton, V.E., Thermal infrared emission spectroscopy of the pyroxene mineral series, *J. Geophys. Res.*, this issue.

Hapke, B., Bidirectional reflectance spectroscopy, 1, Theory, *J. Geophys. Res., 86*, 3039–3054, 1981.

Hunt, G. R., and R. L. Vincent, The behavior of spectral features in the infrared emission from particulate

surfaces of various grain sizes, *J. Geophys. Res.*, *73*, 6039–6046, 1968.

Kieffer, H. H., T. Z. Martin, A. R. Peterfreund, B. M. Jakosky, E. D. Miner, and F. D. Palluconi, Thermal and albedo mapping of Mars during the Viking primary mission, *J. Geophys. Res.*, *82*, 4249–4292, 1977.

Lyon, R. J. P., Analysis of rocks by spectral infrared emission (8–25 microns), *Econ. Geol.*, *60*, 715–736, 1965.

Maguire, W. C., Martian isotopic ratios and upper limits for possible minor constituents as derived from Mariner 9 infrared spectrometer data, *Icarus*, *32*, 85–97, 1977.

Moersch, J. E., and P. R. Christensen, Thermal emission from particulate surfaces: A comparison of scattering models with measured spectra, *J. Geophys. Res.*, *100*, 7465–7477, 1995.

Moersch, J. E., T. L. Hayward, P. D. Nicholson, S. W. Squyres, and J. Van Cleve, Identification of a 10-micron silicate absorption feature in the Acidalia region of Mars, *Icarus*, *126*, 183–196, 1997.

Palluconi, F. D., and H. H. Kieffer, Thermal inertia mapping of Mars from 60 S to 60 N, *Icarus*, *45*, 415–426, 1981.

Pollack, J. B., T. Roush, F. Whitteborn, J. Bregman, D. Wooden, C. Stoker, O. B. Toon, D. Rank, B. Dalton, and R. Freedman, Thermal emission spectra of Mars (5.4–10.5 microns): Evidence for sulfates, carbonates and hydrates, *J. Geophys. Res.*, *95*, 14595–14628, 1990.

Presley, M. A., and P. R. Christensen, Thermal conductivity measurements of particulate materials, 2, Results, *J. Geophys. Res.*, *102*, 6551–6566, 1997.

Ramsey, M. S., and P. R. Christensen, Mineral abundance determination: Quantitative deconvolution of thermal emission spectra, *J. Geophys. Res.*, *103*, 577–596, 1998.

Roush, T., J. B. Pollack, F. Whitteborn, J. Bell III, and B. Sitton, Thermal infrared spectroscopic observations of Mars from the Kuiper Airborne Observatory (KAO): Constraints on past climates and weathering products, in *Airborne Astronomy Symposium on the Galactic Ecosystem: From Gas to Stars to Dust*, edited by H. Haas, J. Davidson, and E. Erickson, Astron. Soc. Pac. Conf. Ser., *73*, 345–348, 1995.

Ruff, S.W., Quantitative thermal infrared emission spectroscopy applied to granitoid petrology, Ph.D. dissertation, Ariz. State Univ., Tempe, 1997.

Salisbury, J. W., B. Hapke, and J. W. Eastes, Usefulness of weak bands in mid-infrared remote sensing of particulate planetary surfaces, *J. Geophys. Res.*, *92*, 702–710, 1987.

Smith, M. D., B. J. Conrath, J. C. Pearl, and P. R. Christensen, Mars Global Surveyor Thermal Emission Spectrometer (TES) observations of dust opacity during aerobraking and science phasing, *J. Geophys. Res.*, this issue.

Thomson, J. L., and J. W. Salisbury, The mid-infrared reflectance of mineral mixtures (7–14 microns), *Remote Sens. Environ.*, *43*, 1–13, 1993.

J. L. Bandfield and P. R. Christensen, Department of Geology, Arizona State University, Tempe, AZ 85287.

M. D. Smith, NASA Goddard Space Flight Center, Code 693, Greenbelt, MD 20771. (Michael.D.Smith.1@gsfc.nasa.gov)

Received June 3, 1999; revised August 11, 1999; accepted August 13, 1999.

This preprint was prepared with AGU's LaTeX macros v5.01. File TES'SAS formatted March 20, 2000.

Figure 1. Typical daytime TES spectra containing only dust with very little contribution from water ice or nonunit surface emissivity. Spectra are shown in terms of brightness temperature. These spectra were taken over Isidis Planitia during the periapsis passes of orbits 61, 93, and 112 (L_s= 234°, 256°, and 266°, respectively).

Figure 2. Derived dust spectral shapes. We adopt the average (solid line) of the spectral shapes from orbits 61, 93, and 112 (L_s= 234°, 256°, and 266°, respectively) as our reference dust spectral shape.

Figure 3. TES spectra containing a large amount of water ice. Spectra are shown in terms of brightness temperature. These spectra were taken near the Arsia Mons volcano during the periapsis passes of orbits 33, 55, and 132 (L_s=210°, 229°, and 276°, respectively).

Figure 4. Derived water-ice spectral shapes. We adopt the average (solid line) of the spectral shapes from orbits 33, 55, and 132 (L_s= 210°, 229°, and 276°, respectively) as our reference water-ice spectral shape.

Figure 5. Relative opacities of dust and water-ice aerosols along the orbit 55 (L_s=229°) periapsis pass. These opacities are obtained for each spectrum by performing a least squares minimization to find the best fitting scaling factors given the previously retrieved (and fixed) dust and water-ice spectral shapes. The topographic profile stands out in reverse in the dust opacity. There are large discrete water-ice clouds near the summit and on the southern flank of Arsia Mons. The residual is low throughout, indicating that the TES observed opacities are well fit by dust and water ice alone.

Figure 6. Relative opacities of dust and water-ice aerosols along the orbit 219 (L_s=305°) periapsis pass. There is a well-defined region of high residual between 15° and 35°S latitude. In this region the TES-observed opacities are not well fit by dust and water ice alone. A nonunit emissivity surface is required to fit the observations.

Figure 7. Derived surface emissivity spectral shape for orbit 219 (L_s= 305°) spectra taken over Terra Cimmeria (15°–35°S, 212°W). This spectral shape is in terms of emissivity, not in terms of opacity as with the dust and water-ice spectral shapes shown in Figures 2 and 4.

Figure 8. As in Figure 6, except that now a surface with emissivity spectral shape shown in Figure 7 is also fit. The area of high residual seen in Figure 6 directly corresponds to the region where there is a significant surface contribution.

Figure 9. Derived surface emissivity spectral shape for orbit 219 (L_s= 305°) spectra taken over Terra Cimmeria (15°–35°S, 212°W) for each of the six TES detectors. The data from each detector makes up an independent data set, and so the spread in these curves gives an indication of the uncertainties involved in the Radiative Transfer Algorithm.

Figure 10. The original basaltic spectrum (solid line) can be accurately recovered (dashed-dotted line) from the nonlinear emissivity-transmissivity system using a linear approximation. The residual error with a baseline of 1 is shown for reference.

Figure 11. Atmospheric components isolated from orbit 219 (L_s= 305°). Dust is shown as the solid line, and water ice is shown as the dashed-dotted line. The shapes have been normalized from 0 to 1. Note the presence of weak CO_2 absorptions, especially at 1064 cm^{-1}, and the numerous water vapor absorptions between 200 and 400 cm^{-1} present in the dust spectral shape.

Figure 12. Result of the linear least squares fit using the dust and water-ice spectral shapes shown in Figure 11 as well as a suite of 60 mineral spectra. The original TES spectrum (solid line) is modeled closely (dashed-dotted line) with an RMS error of 0.00232.

Figure 13. The measured (solid line) and modeled spectra (dashed-dotted line) with the derived concentrations of atmospheric water ice and dust removed. The mineral suite can model the surface spectrum closely. Analysis of the surface spectral signature and the derived mineral percentages are discussed by *Christensen et al.* [this issue (a)].

Figure 14. Comparison of dust and water-ice spectral shapes obtained by the Radiative Transfer and the Deconvolution Algorithms. The agreement is very good. Differences in the dust spectral shapes are caused by CO_2 hot bands at 1075 cm^{-1} and by the difference between an opacity (used by the Radiative Transfer Algorithm) and an emissivity (used by the Deconvolution Algorithm) representation for the spectral shapes at 300–575 cm^{-1}.

Table 1. Key Parameters for the Sets of Data Used in This Analysis

Orbit	Icks[a]	Lat	Long	LT[b]	T_{surf}[c]	Range[d]	Emis[e]
			Dust Spectral Shape				
61	775–800	7°–11°N	276°W	15.1	255	336–392	4–5
93	795–834	10°–15°N	269°W	13.6	265	322–408	2–4
112	905–935	11°–21°N	263°W	12.9	260	584–672	48–70
			Water-Ice Spectral Shape				
33	1224–1362	21°–7°S	122°W	16.6	245	656–1122	0–1
55	993–1043	16°–7°S	122°W	15.3	275	994–1178	19–36
132	1198–1235	8°S–11°N	118°W	12.2	290	1198–1235	35–70
			Surface Emissivity Spectral Shape				
56	1021–1121	27°–10°S	214°W	15.3	285	1056–1440	1–32
219	1585–1675	25°–12°S	212°W	10.1	275	1520–1848	20–31

[a]TES uses "icks" to count event time during an orbit. They are used to identify spectra. Each ick is 2 s in duration.

[b]LT is local time measured in a 24 hour Martian day beginning at midnight.

[c]T_{surf} is the approximate average surface temperature (K) for these icks.

[d]Range is the perpendicular distance from the surface in kilometers.

[e]Emis is the emission angle measured in degrees.

Plate 1. Comparison of surface emissivity spectral shapes obtained by the Radiative Transfer and the Deconvolution Algorithms. Here, all spectral shapes are in an emissivity representation and so are directly comparable. Orbits 56 and 219 (L_s= 230° and 305°, respectively) are separated by about 2° in longitude (Terra Cimmeria). The fifth (purple) shape was obtained by the Radiative Transfer Algorithm with the additional assumption that water-ice opacity is zero. The difference between the curves gives an indication of the uncertainties associated with the two algorithms.

↑ TOP

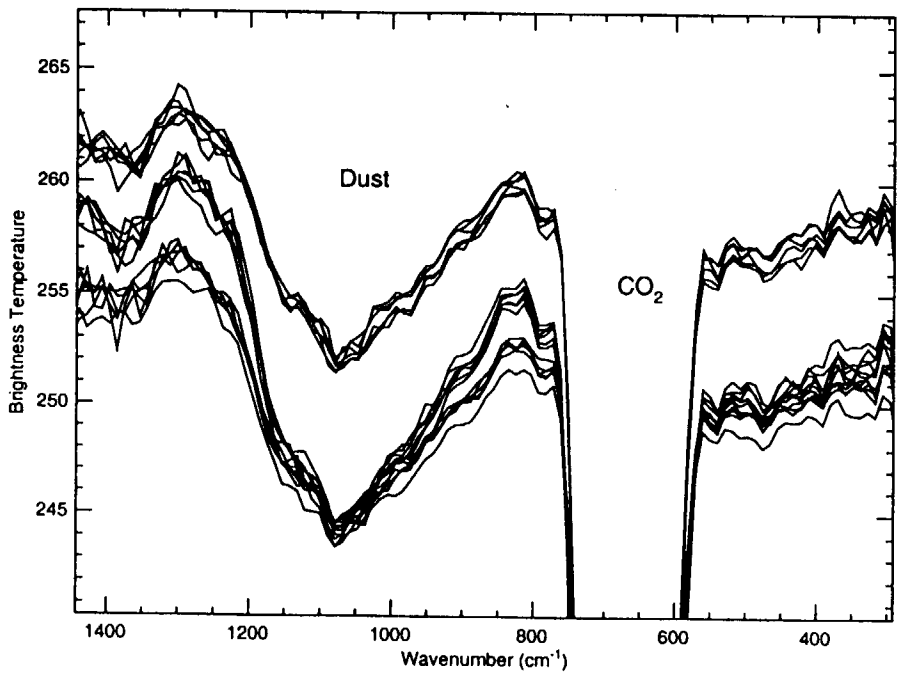

SMITH ET AL.
1999JE001105
FIG. 1

↑ TOP

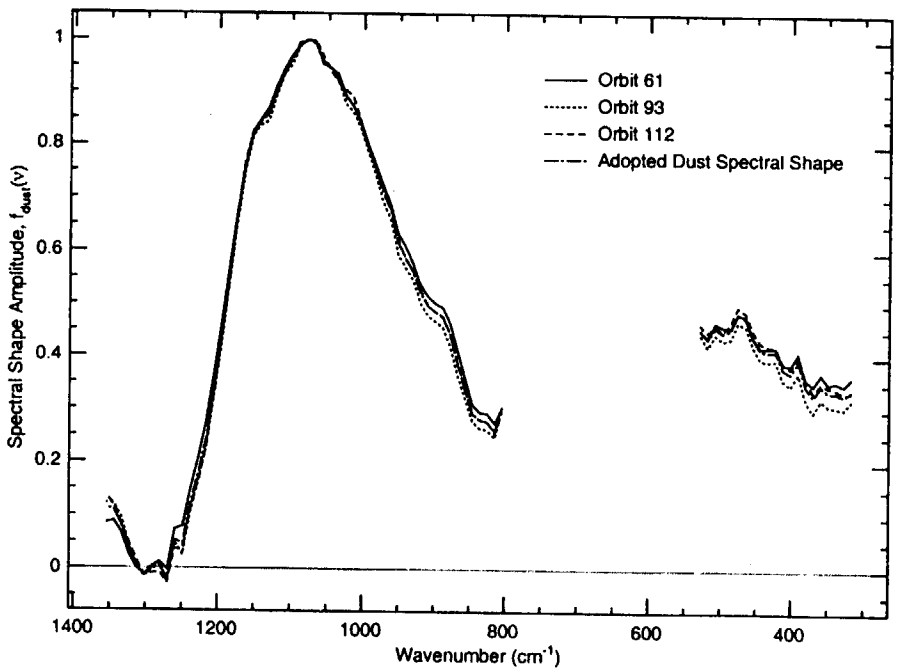

SMITH ET AL.
1999JE001105
FIG. 2

↑ TOP

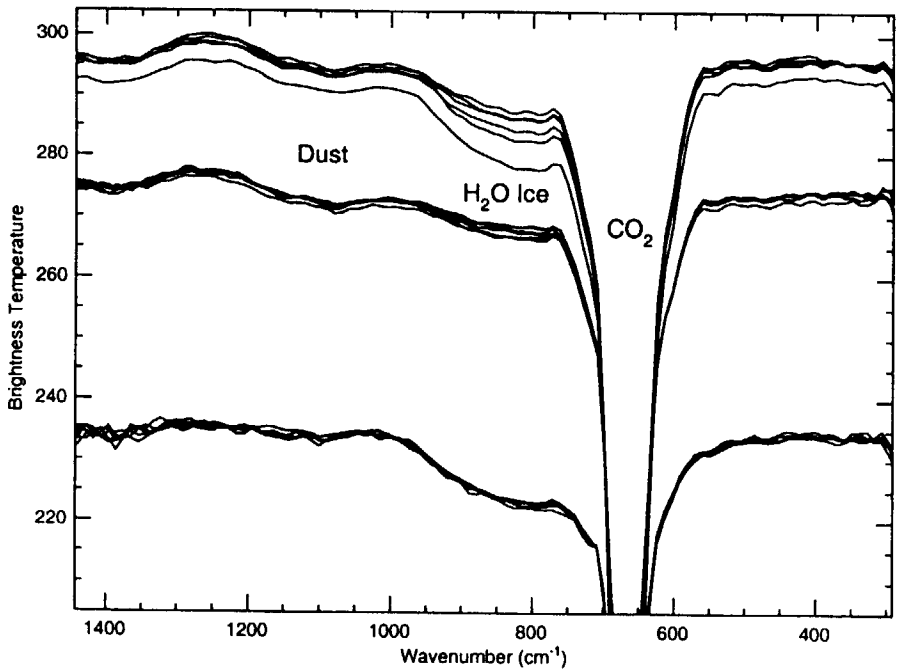

SMITH ET AL.
1999 JE001105
FIG. 3

TOP

SMITH ET AL.
1999JE001105
FIG. 4

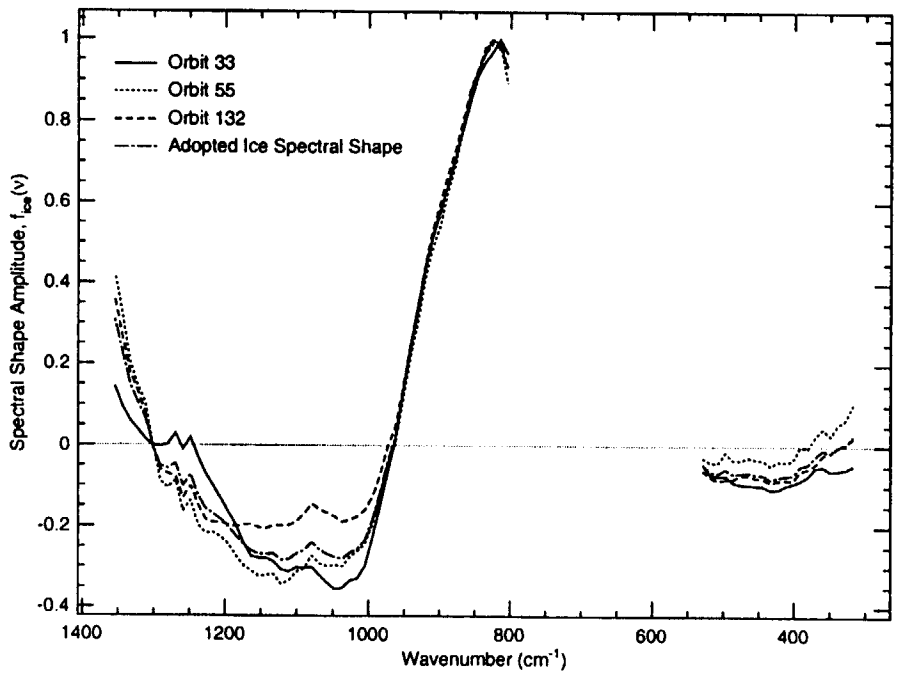

TOP

SMITH ET AL.
1999JE001105
FIG. 5

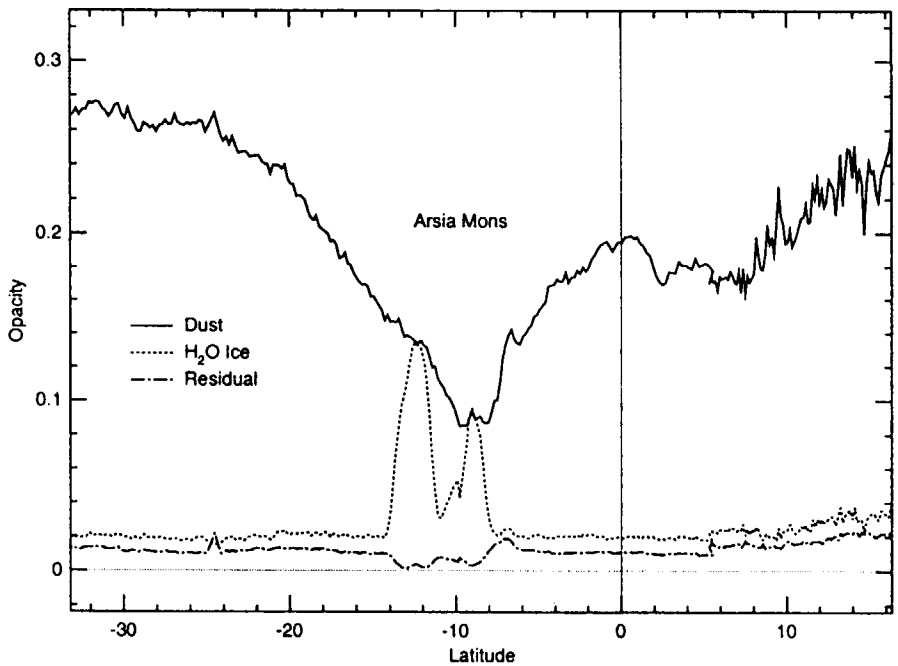

TOP

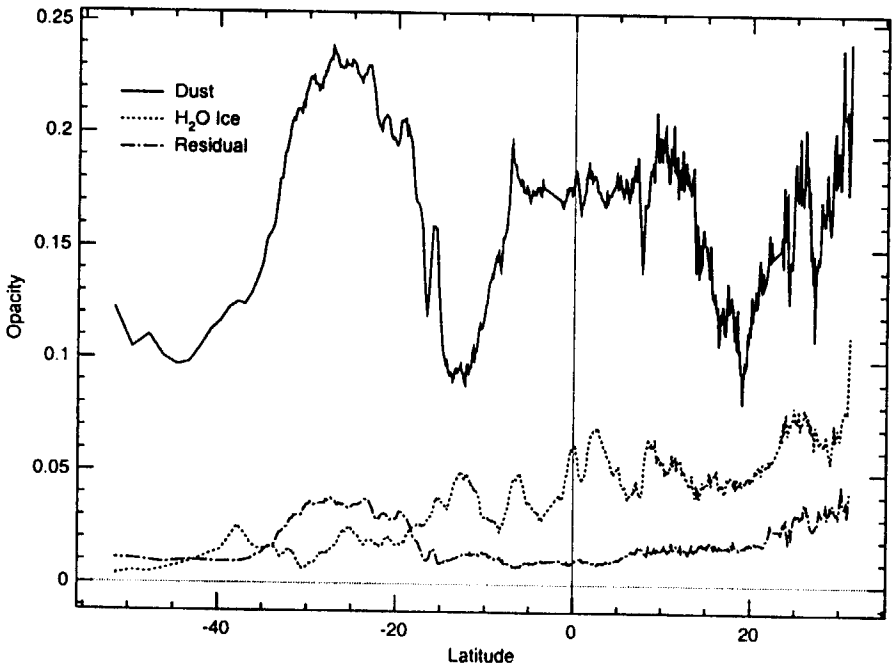

SMITH ET AL.
1999JE001105
FIG. 6

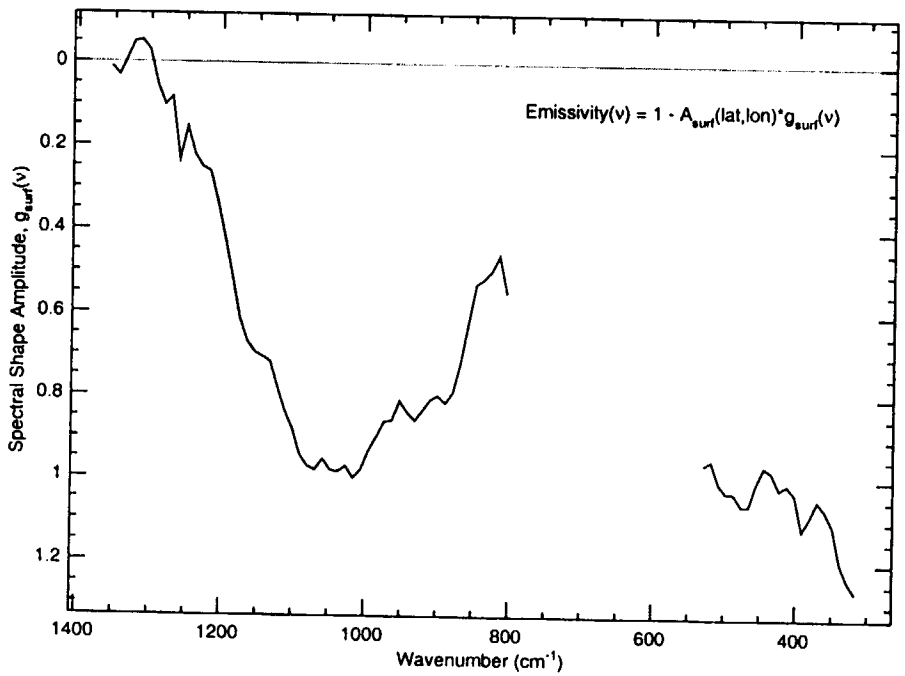

TOP

SMITH ET AL.
1999JE001105
FIG. 7

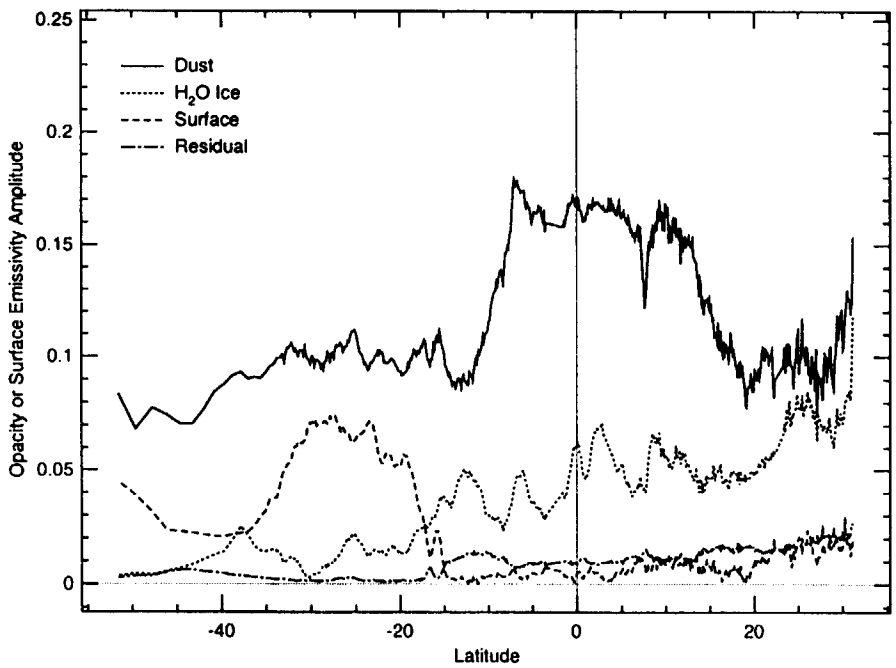

TOP

SMITH ET AL.
1999JE001105
FIG. 8

↑ TOP

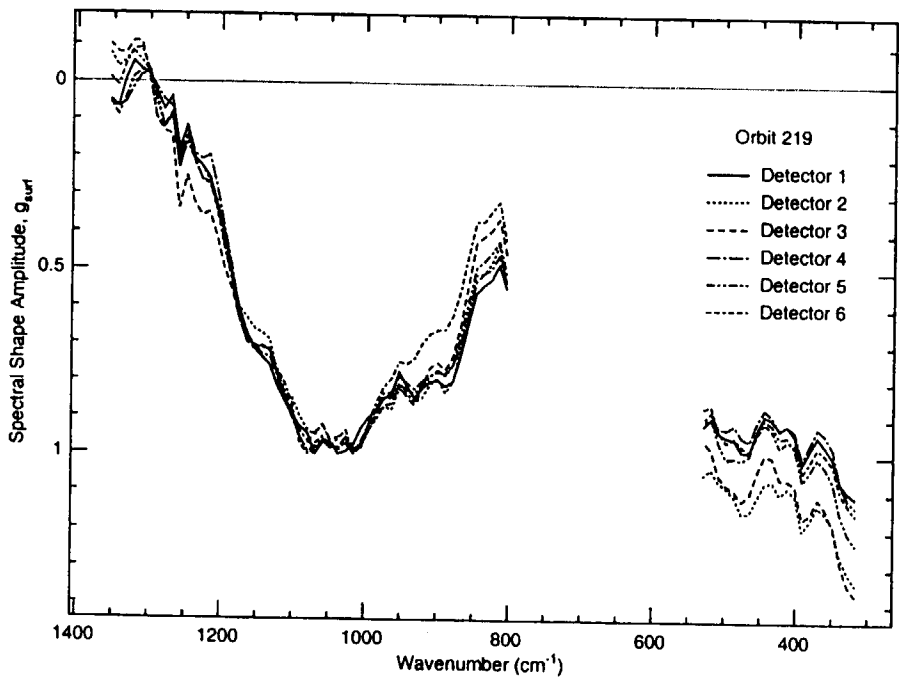

SMITH ET AL.
1999JE001105
FIG. 9

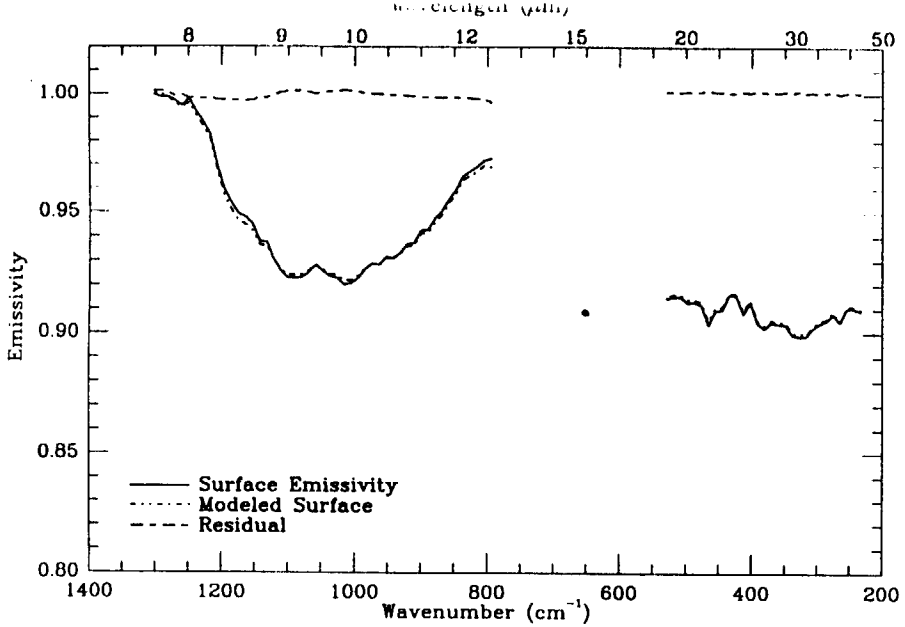

TOP

SMITH ET AL.
1999JE001105
FIG. 10

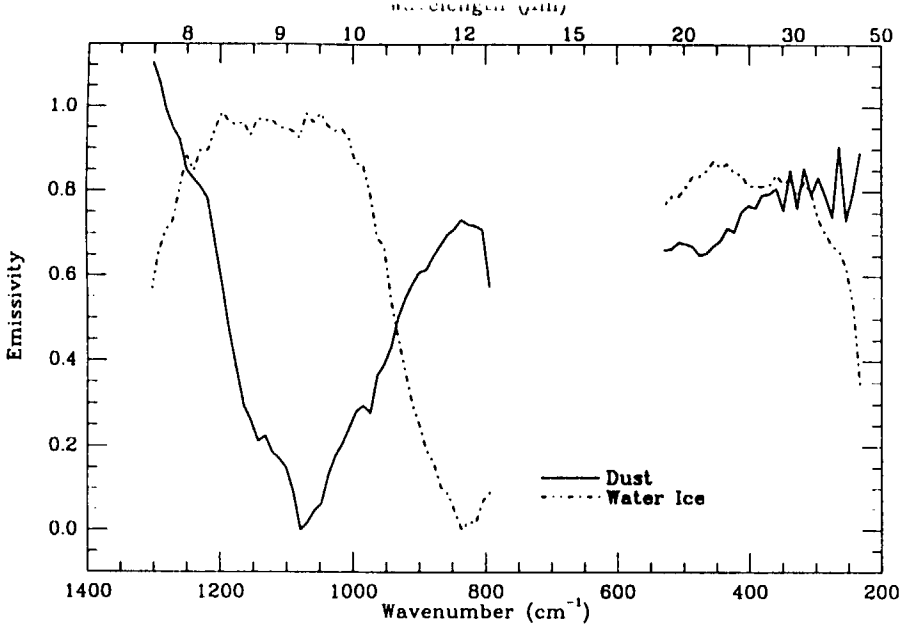

TOP

SMITH ET AL.
1999JE001105
FIG. 11

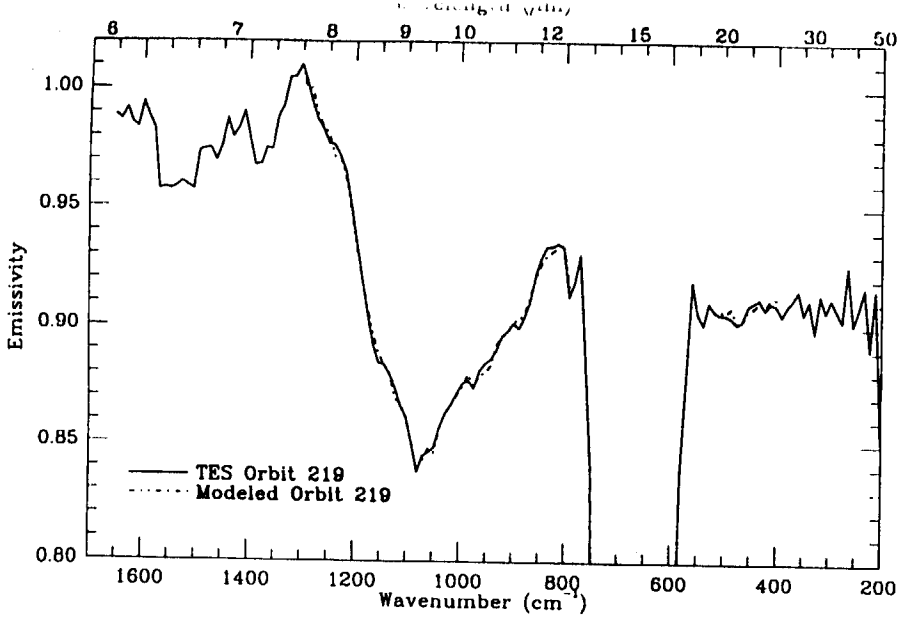

TOP

SMITH ET AL.
1999JE001105
FIG. 12

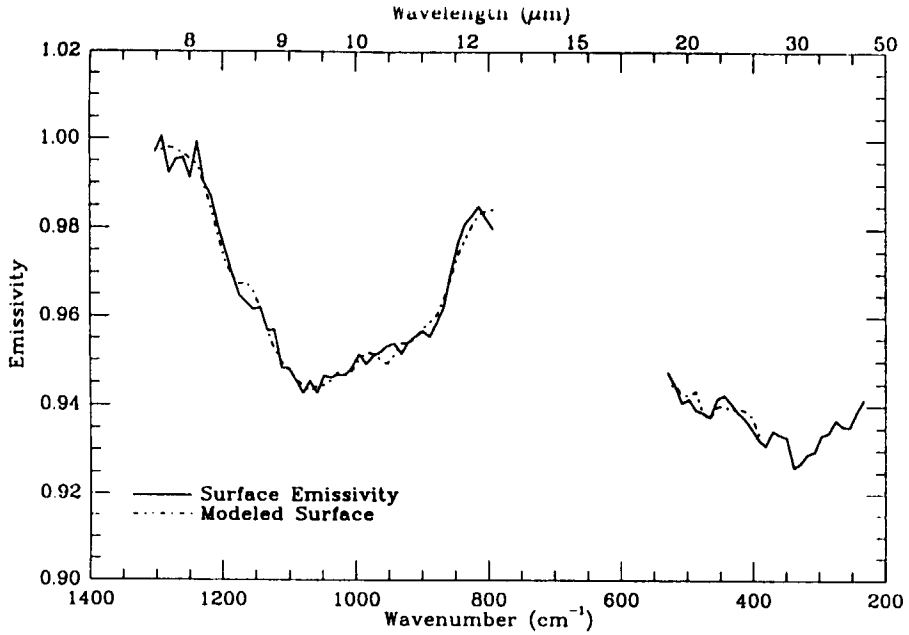

TOP

SMITH ET AL.
1999JE001105
FIG. 13

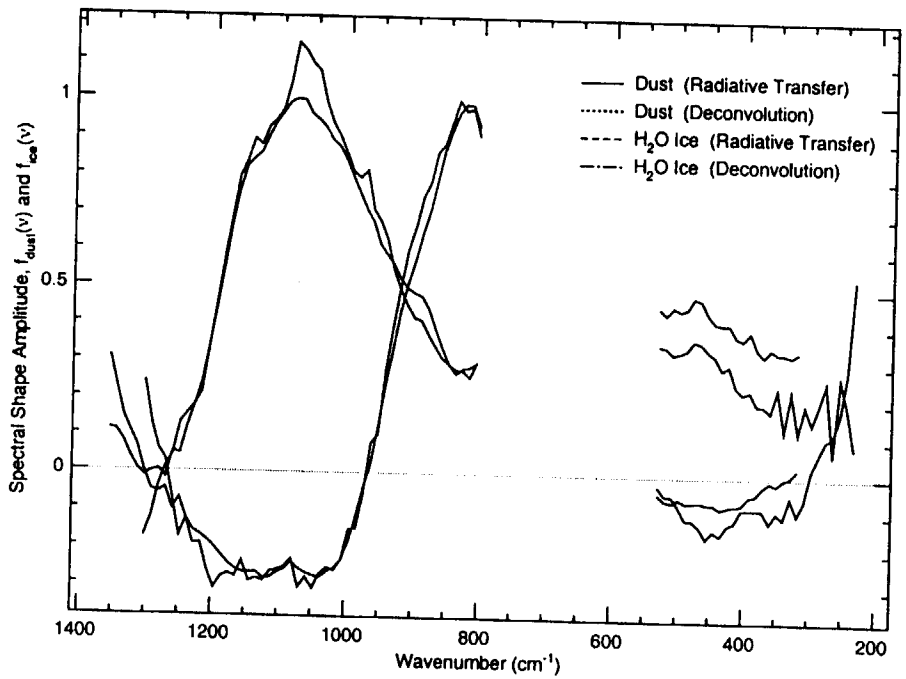

SMITH ET AL.
1999JE001105
FIG. 14

Plate 1

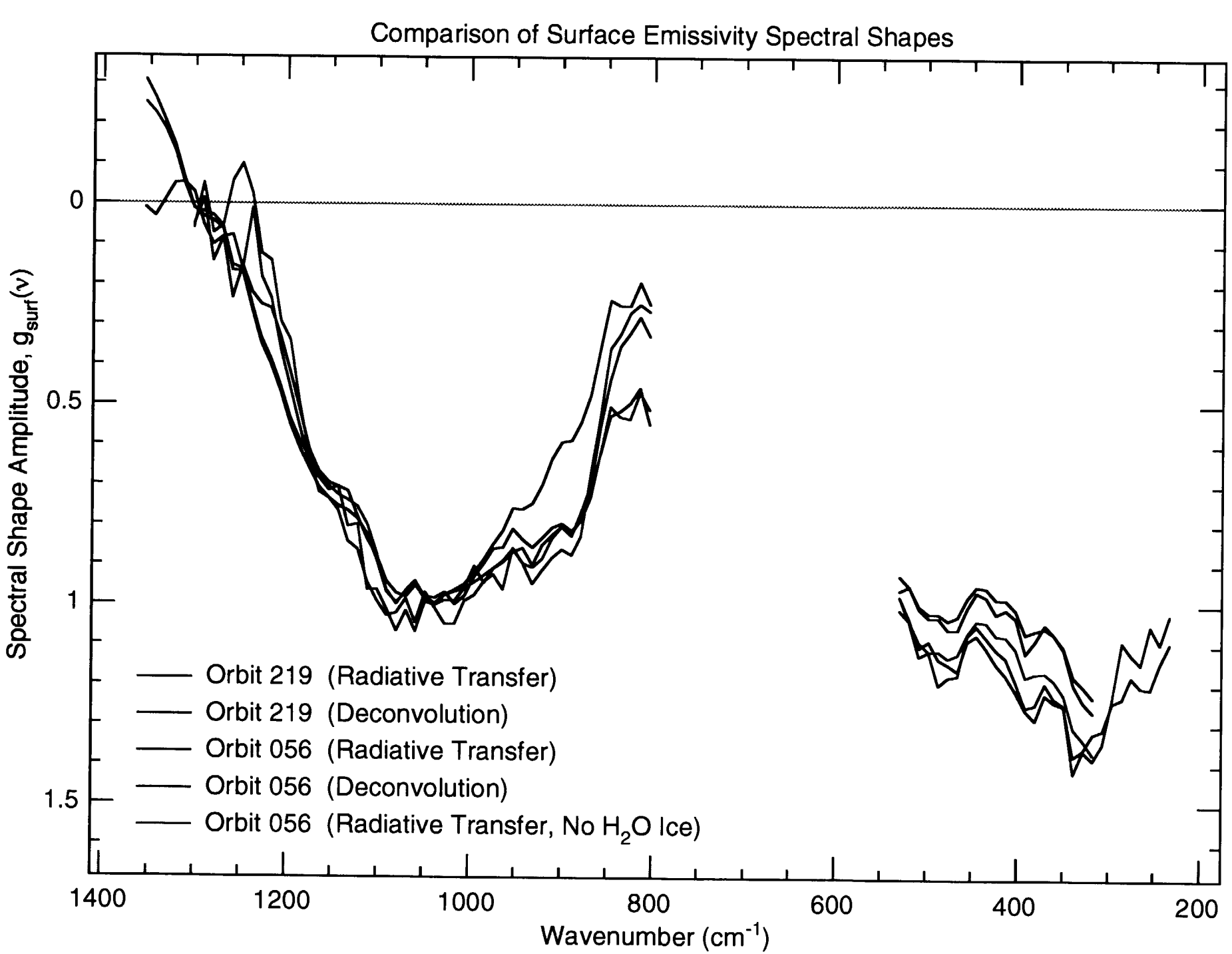
Comparison of Surface Emissivity Spectral Shapes
Spectral Shape Amplitude, $g_{surf}(\nu)$
0
0.5
1
1.5
1400
1200
1000
800
600
400
200
Wavenumber (cm^{-1})
Orbit 219 (Radiative Transfer)
Orbit 219 (Deconvolution)
Orbit 056 (Radiative Transfer)
Orbit 056 (Deconvolution)
Orbit 056 (Radiative Transfer, No H_2O Ice)